Title
The Non-Traditional Coriolis Terms and Tropical Convective Clouds

Journal
Journal of the Atmospheric Sciences, 77(12)

ISSN
0022-4928

Authors
Igel, Matthew R
Biello, Joseph A

Publication Date
2020

DOI
10.1175/jas-d-20-0024.1

Journal of the Atmospheric Sciences

The Non-Traditional Coriolis Terms and Tropical Convective Clouds

--Manuscript Draft--

Manuscript Number:	JAS-D-20-0024
Full Title:	The Non-Traditional Coriolis Terms and Tropical Convective Clouds
Article Type:	Article
Corresponding Author:	Matthew R Igel, PhD University of California Davis Davis, CA UNITED STATES
Corresponding Author's Institution:	University of California Davis
First Author:	Matthew R Igel, PhD
Order of Authors:	Matthew R Igel, PhD
	Joseph Biello, PhD
Abstract:	The full, three-dimensional Coriolis force includes the familiar sine-of-latitude terms as well as frequently dropped cosine-of-latitude terms (Nontraditional Coriolis Terms [NCT]). The latter are often ignored because they couple the zonal and vertical momentum equations which in the large-scale limit of weak vertical velocity is insignificant almost everywhere. Here, we ask whether equatorial clouds which fall outside the large-scale limit are affected by the NCT. A simple scaling indicates that a parcel convecting at 10m/s through the depth of the troposphere should be deflected over 2km to the west. An initial set of cloud resolving simulations indicate a preferential lifting of surface parcels with positive zonal momentum and stronger convection on the western side of convective updrafts. To explain these results, we develop a mathematical framework which incorporates an azimuthally symmetric convective circulation with an incompressible poloidal flow. Because the model incorporates the full 3-dimensional flow associated with convection, it uniquely predicts not only a force acting to tilt clouds westward but also a force acting to spread upper-level outflow meridionally. These predictions are confirmed with an additional pair of cloud resolving simulations designed to mimic the steady-state flow of the model. Results suggest the NCT are impactful to equatorial mesoscale convective circulations.
Suggested Reviewers:	Hing Ong hwang2@albany.edu

The Non-Traditional Coriolis Terms and Tropical Convective Clouds

Matthew R. Igel*

Department of Land, Air and Water Resources, University of California Davis, Davis, California

Joseph A. Biello

Department of Mathematics, University of California Davis, Davis, California

**Corresponding author*: Matthew R. Igel, migel@ucdavis.edu

ABSTRACT

The full, three-dimensional Coriolis force includes the familiar sine-of-latitude terms as well as frequently dropped cosine-of-latitude terms (Nontraditional Coriolis Terms [NCT]). The latter are often ignored because they couple the zonal and vertical momentum equations which in the large-scale limit of weak vertical velocity is insignificant almost everywhere. Here, we ask whether equatorial clouds which fall outside the large-scale limit are affected by the NCT. A simple scaling indicates that a parcel convecting at $10\,\mathrm{m s^{-1}}$ through the depth of the troposphere should be deflected over 2km to the west. An initial set of cloud resolving simulations indicate a preferential lifting of surface parcels with positive zonal momentum and stronger convection on the western side of convective updrafts. To explain these results, we develop a mathematical framework which incorporates an azimuthally symmetric convective circulation with an incompressible poloidal flow. Because the model incorporates the full 3-dimensional flow associated with convection, it uniquely predicts not only a force acting to tilt clouds westward but also a force acting to spread upper-level outflow meridionally. These predictions are confirmed with an additional pair of cloud resolving simulations designed to mimic the steady-state flow of the model. Results suggest the NCT are impactful to equatorial mesoscale convective circulations.

1. Introduction

In a typical introductory atmospheric dynamics class, students often derive the full form of the Coriolis force – the apparent force introduced by formulating our equations of motions in a non-inertial reference frame (de Coriolis 1835; Poisson 1838) attached to the rotating Earth. In three dimensions, in a rotating frame of reference, the momentum equations for an inviscid fluid are

$$\frac{Du}{Dt} + \frac{\partial p}{\partial x} = 2\Omega \sin(\phi) v - \underline{2\Omega_0 \cos(\phi) w} \tag{1}$$

$$\frac{Dv}{Dt} + \frac{\partial p}{\partial y} = -2\Omega_0 \sin(\phi) u \tag{2}$$

$$\frac{Dw}{Dt} + \frac{\partial p}{\partial z} = \underline{2\Omega_0 \cos(\phi) u} + B. \tag{3}$$

In (1)-(3), u, v, and w are the vector components of the wind, Ω_0 is the rotation rate of the Earth, and ϕ is the latitude, p is the geopotential, the analog of the pressure for incompressible flows, and B is the force of gravity, associated with buoyancy. In order to specify the geopotential, we require another equation. When the Mach number of the flow is small - as is relevant at convective scales in the atmosphere, pressure waves travel quickly, and the flow can be described through either the anelastic or incompressible approximation. In order to simply the discussion, we will use the incompressible approximation in what follows

$$\frac{\partial u}{\partial x} + \frac{\partial v}{\partial y} + \frac{\partial w}{\partial z} = 0, \tag{4}$$

and the generalization to anelastic flows will be straightforward from the incompressible theory. Equations (1)-(4) describe the motion of an ideal fluid under the "full Coriolis force".

In an effort to meaningfully simplify the standard equations of motion, we often use scaling arguments which suggest that, in typical midlatitude conditions, the underlined term on the RHS of (1) is much smaller than the first, and so can be neglected. We then note that the underlined term on the right hand side of (3) is much smaller than the leading order vertical accelerations, gravity and the pressure gradient force. These assumptions lead to the so-called “Traditional Approximation” of the Coriolis force. For standard, synoptic, midlatitude meteorology, the traditional approximation does not introduce any major errors. However, at or near the equator, these approximations are inaccurate due to the relative largeness of $\cos(\phi)$ compared to $\sin(\phi)$, all other magnitudes being equal. The underlined terms in (1)-(3) are sometimes called the “Non-traditional Coriolis Terms” (NCT) being derived from the “Non-traditional Approximation” of the Coriolis force.

Of course, we are not the first to discuss the form or impact of the NCT. The NCT are commonly considered in hydrodynamic flows of deep-atmosphere planets (Savonije and Papaloizou 1997; Ogilvie and Lin 2004; Dintrans et al. 1999) and sometimes on terrestrial ocean dynamics (Denbo and Skyllingstad 1996; Marshall and Schott 1999). Their effect on the atmosphere is less commonly considered although reasonably well understood in some contexts. Hayashi and Itoh (2012) examine the off-equatorial response of an MJO-like diabatic heating forced by the NCT. Ong and Roundy Ong and Roundy (2019) recently examined the response of equatorial synoptic flows to the NCT in a simplified model. Tort and Dubos Tort and Dubos (2014) developed a shallow water model for the complete Coriolis force. What these papers all have in common, besides a near universal message not to ignore the NCT, is a minimum length scale and time scale of consideration. Below the synoptic scale in the atmosphere, the NCT have received little systematic attention.

In this paper, we ask a simple question about the NCT: what is its impact on tropical convective circulations? Part of the motivation for asking this question is practical. For example, the WRF documentation (`http://www2.mmm.ucar.edu/wrf/users/docs/arw_v3.pdf`; pg 11) states that for a standard Cartesian grid, the accelerations due to the NCT should be set to zero [1]. But if the impact of the NCT on the kinds of cloud resolving simulations for which WRF was designed is consequential, WRF users may need to consider the impact of these ignored terms. CM1 (Bryan 2015) also assumes the NCT are zero (as of version 19.2). RAMS (Cotton and Coauthors 2003; Saleeby and Cotton 2008) does not include the NCT. NICAM (Satoh et al. 2010) does include these terms – so their exclusion is not universal among cloud models. And, it has been argued that as grid spacing shrinks in global models, NCT should be added there as well (Kasahara 2003).

That being said, we are more generally motivated by a suspicion that the NCT may play an underappreciated role in shaping the evolution of equatorial convective circulations and the resultant morphology of convection. In the preamble to their review of the impact of the NCT on geophysical flows, Gerkema et al. (2008) lament that,"[as] the interest in [NCT] has waxed and waned repeatedly, the literature is scattered, and much of it has slipped into oblivion". Therefore, we think it is plausible that the NCT has been unintentionally ignored at the atmospheric mesoscales.

In order to answer our motivating question, we rely on cloud modeling and analytic results. These are organized as follows. First, we examine the equatorial scales of motion implied by the NCT. Then we attempt to simulate the impact of the NCT in two cases: one will show the asymmetric impact zonal velocity has on convective motions and the other will show the impact of the NCT on the statistics of clouds and precipitation. Next, we develop an analytic model for the impact of the NCT on closed equatorial circulations. This analytic model uses an important intuition - pressure waves travel much more quickly than convective flows, so the atmosphere in the vicinity of a convective flow behaves incompressibly (more accurately, anelastically). Pressure in

[1] The Coriolis underlined terms on the RHS of (1) and (3) are listed in that documentation as "curvature terms" instead of "Coriolis term". In a broad sense, this is merely a semantic choice by the document's authors, but we would argue against this choice given that curvature terms are not merely the result of changing one's reference frame as Coriolis terms are.

incompressible flows, is determined diagnostically through the Leray projection. Using the Leray projection, we explicitly describe the force on a model convective flow. The mathematics works out extremely simply and shows one component of the force (we call it the Coriolis Rotation term) to be proportional to the sine of the longitude which drives the traditional cyclonic/anticyclonic motion associated with convection. The second component of the force is proportional to the cosine of the longitude, is strongest in the tropics, and is therefore the primary effect of the NCT. This Coriolis Shear force, as we call it, is westward in the ascending part of a convective flow and diffluent at the top of the circulation. Finally, we test this new analytic model with a pair of steady-state simulations designed to mimic the model.

2. Exploratory Results

a. Inertial Circles

As a suggestive practice, we examine the nature of inertial circles induced by the NCT. If one considers an air parcel of always-neutral buoyancy that instantaneously adjusts to the local pressure, then (1)-(3) can be simplified and integrated in time to yield: $U(t) = U_0 \sin(2\Omega_0 \cos(\phi)t)$ and $W(t) = W_0 \cos(2\Omega_0 \cos(\phi)t)$. The dots in Fig. 1 mark the path of an initially slowly eastward moving ($U_0 = 1\,\mathrm{ms}^{-1}$, $W_0 = 0\,\mathrm{ms}^{-1}$) parcel. Only the NCT act on this parcel. Over the course of 12 hours, the parcel traces out a 1400m wide circle and returns to its initial location. The parcel maintains its initial speed throughout the oscillation. In an idealized sense, this oscillation may be imaged as a simple Taylor column aligned with the rotation axis of the planet, which at the equator is perpendicular (i.e. into the page) to the local vertical (Gerkema et al. 2008; Busse 1976).

The diamonds in Fig. 1 show the evolution of a westward moving ($U_0 = -1\,\mathrm{ms}^{-1}$, $W_0 = 0\,\mathrm{ms}^{-1}$) parcel initially 1km above the surface. These are identical conditions to the first parcel save for the sign of zonal momentum. In this case, the parcel descends until it reaches the surface. At that time, its vertical momentum is transferred to the surface (by construction in our simple example), but its zonal momentum is unaffected. The parcel then skids along the surface with constant momentum thereafter. So, the behavior of two parcels with identical initial properties, except for the sign of their zonal velocity, is very different when influenced by the NCT and subject to a rigid surface. Of course, these examples are contrived and do not include all kinds of real world complexity inherent in parcel motion. That being said, the point they make well is that the NCT have the potential to act asymmetrically; a concept that we will reiterate below.

b. Simple Scaling

Next, we will suggest that the impact of (1)-(3) may be non-negligible at the mesoscale. The zonal displacement due to a constant acceleration and zero initial velocity in the zonal direction over a period, Δt, is, of course,

$$\Delta X = \frac{1}{2}\frac{Du}{Dt}\Delta t^2. \tag{5}$$

If we assume that an arbitrary parcel ascends with constant vertical wind speed, W, over a depth of atmosphere, H, then

$$\Delta X = -2\Omega_0 cos(\phi)\frac{H^2}{W}. \tag{6}$$

Equation (6) suggests that a zonal displacement of an ascending air parcel depends on the square of the depth of the ascent and inversely on the velocity. We will consider two cases relevant to the tropical atmosphere. The first is of a convecting, cloudy parcel. In this case, $H = 18\,\mathrm{km}$ and $W = 10\,\mathrm{ms}^{-1}$. This implies $\Delta X = -2.4\,\mathrm{km}$. Taken literally, this would suggest that up to 2.4km of the lateral deflection of a cloudy parcel is due purely to Coriolis acceleration. This deflection would mean that convection is not upright but rather tilted at 7.5% with the vertical toward the west.

The second case is one of a subsiding, clear air parcel. In this case, $H = 18\,\mathrm{km}$ and $W = -0.10\,\mathrm{ms^{-1}}$. This implies $\Delta X = 240\,\mathrm{km}$. Because of the inverse dependence of the displacement on the magnitude of W, the slowly subsiding parcel is displaced more than the relatively quickly convecting parcel.

The change in speed of a parcel ascending over a depth of atmosphere is

$$\Delta U = -2\Omega_0 cos(\phi) H. \tag{7}$$

Equation (7) shows that unlike for the displacement of a parcel, the final velocity does not depend on vertical velocity such that ascending and descending parcels gain the same speed, although they are in opposite directions. The zonal velocity of a parcel that ascends through the depth of the tropical troposphere is slowed by $2.6\,\mathrm{ms^{-1}}$.

c. Initial RAMS Simulations

1) Isolated Congestus Simulations

Of course, both (6) and (7) are over-estimates of potential effects on real-world parcels which are subjected to friction and pressure forces. So next, we will add the NCT to the RAMS model (Cotton and Coauthors 2003) which will be run here in a cloud-resolving configuration. Our first set of simulations are run on an isotropic grid of 150 m spacing on a domain of 45 km on a side and 21 km tall. The simulations are initialized with a mean sounding from the DYNAMO field campaign (Ciesielski et al. 2014) with a slightly moistened boundary layer to help sustain moist convection. We use the RAMS double moment (Igel et al. 2015), bin-emulating microphysics (Saleeby and Cotton 2004; Saleeby and van den Heever 2013), cyclic lateral boundaries, 20 damping layers at model top, and no radiation.

We ran six simulations. Three each on an equatorial f-plane with (1)-(3) included (NCT_{on}) and three with the standard RAMS equation set (NCT_{off}). The three simulations differed in their intensity of the boundary layer convergence that was included in the model to excite convection. The intensities of convergence were: $4.0 \times 10^{-4} s^{-1}$, $2.5 \times 10^{-4} s^{-1}$, and $1.5 \times 10^{-4} s^{-1}$. We also tried $0.5 \times 10^{-4} s^{-1}$, but it failed to excite sustained convection. We will focus on the onset of convection in these simulations while simulations are directly comparable.

To make use of this mini-ensemble of LES, we will show the ensemble, time-integrated mean of physical quantities for 20 minutes of simulation. All three simulations within a set are averaged together to best ensure results are general and not just the result of numerical noise. Figure 2a/b shows the ensemble-mean zonal and vertical winds. These figures show the wind is convergent at the surface and convective from just above the surface to at least 4km. Figure 2c/d show differences of these quantities between the two simulations (taken as NCT_{on} minus NCT_{off}). These difference plots show two results that are not necessarily obvious from examining (1) and (3). First, zonal wind differences at the surface are uniformly negative. Second, there is a coherent, though somewhat noisy, velocity couplet in the vertical wind difference.

We take these noted differences to be simulated examples of the symmetry breaking discussed in section 2a. The negative zonal velocity difference at the surface is the result of preferential lifting of parcels with positive zonal velocities and preferential sinking (in this case, to the ground) of parcels with negative zonal momentum. Figure 2d illustrates the impact of (3); air with positive zonal momentum has higher vertical velocity up to about 3 km height. The maximum magnitude of the velocity differences is approximately 1% of the magnitude of the composite velocities. While the impact of the NCT on short-lived convection appears to be weak, we want to stress that it is systematic.

2) Radiative Convective Equilibrium Simulations

We also ran two sets of radiative convective equilibrium (RCE) simulations. New simulations were run starting after day 60 of the RCE simulations from Igel (2018). We ran for an additional ten days. Simulations were performed with a 200km square, doubly-periodic domain with 1km spacing and 65 vertical levels with stretched spacing (see 3). At the time of the restart, all the RAMS thermodynamic variables, including hydrometeor species, were used to initialize the new run but the dynamic fields were universally set to zero. We reset the dynamic fields to eliminate the imprint of any mean flow that may have developed in the 60 day run. It did not take long for the simulation to spin up new kinetic energy similar to the behavior seen in (Colin et al. 2018). We ran two simulations, RCE_{on} and RCE_{off}, where "on" and "off" refers to the NCT. We show results averaged over the final five days of these simulations.

Figure 3 shows the average convective vertical velocity conditioned on a minimum of $1\,\mathrm{m\,s^{-1}}$. Unlike in the LES, the RCE statistics indicate weaker convective strength throughout the depth of the convecting layer. The magnitude of the difference is surprisingly large at approximately $2\,\mathrm{m\,s^{-1}}$. The structural difference in the velocity profile is the height of the maximum. In RCE_{on}, the maximum vertical velocity occurs at around 6 km; in RCE_{off}, there is a local maximum near the same altitude but the global maximum occurs much higher at around 11km. Solid dots are included in Figure 3 to indicate levels at which vertical velocity distributions in RCE_{on} and RCE_{off} are statistically different as determined by a two-sided t-test at the 99% level. Convective vertical wind distributions are distinguishable at every level below 15 km.

Next, we contrast the nature of precipitation in RCE_{on} with RCE_{off}. We do this by constructing composite surface precipitation intensity maps from the instantaneous output from RAMS. Maps are constructed so that the maximum precipitation value occurring within a contiguous region of precipitation intensity greater than or equal to $1\,\mathrm{mm\,hr^{-1}}$ occurs in its middle. All precipitation values outside this region are zeroed. Because of the doubly periodic nature of the RCE simulations, maps are padded out on all sides and then pared back to the size of the simulation grid (200km x 200km) centered on the precipitation maximum. Figure 4a shows that precipitation intensity is weakened most significantly just to the east of the composite centroid. This is consistent with weakened vertical velocities on the eastern side of convection shown in section 2c1.

Figure 4b shows the azimuthally averaged, mean structure of precipitation intensity. In $\mathrm{RCE_{off}}$, maximum mean precipitation falls at approximately $15\,\mathrm{mmhr^{-1}}$ while in $\mathrm{RCE_{on}}$, the maximum intensity is only $12\,\mathrm{mmhr^{-1}}$. This could simply be a consequence of the decrease in maximum updraft speeds (Fig. 3). Or, it could be due to a change in the structure of clouds. Figure 4 shows that while the peak intensity of composite precipitation in $\mathrm{RCE_{on}}$ is lower, rain rates are actually higher beyond 10 km from the composite center. The right axis of Fig. 4 helps to show the importance of this difference. It indicates the total accumulation that occurs at any distance from the center (essentially just a distance-squared weighting). The peak accumulation occurs 5 km from the composite storm centers and is 25% higher in $\mathrm{RCE_{off}}$. But beyond 12 km, $\mathrm{RCE_{on}}$ storms have as much as 300% more accumulation (due to small accumulation in $\mathrm{RCE_{off}}$). That is, precipitation features are much wider in $\mathrm{RCE_{on}}$. An approximate visual-integration of the red curves indicates the total precipitation accumulation in the composite storm in $\mathrm{RCE_{off}}$ and $\mathrm{RCE_{on}}$ are nearly the same (they are, indeed, within 1% of one another).

3. The NCT and Complete Convective Circulations

The simple scaling in section 2b is convenient but fundamentally flawed as it employs simple "parcel" thinking. Real convection occurs in a continuous fluid which means air movement causes pressure perturbations. The simulation results in section 2c show that the effects of the NCT are not simply to introduce inertial oscillations within the cloud field. Simulation results often present logical consequences of the NCT, but they fail to suggest any kind of unified model. It is our supposition that complicated consequences of the NCT arising from even subtle indirect impacts of the NCT on the pressure field will be consequential to the complicated mesoscale evolution of convection. Not only will it result in behavior different than the simple scaling indicates in the vertical-zonal plane, but it will also have the potential to impact meridional flow since pressure is isotropic. Indeed, we observed some evidence of meridional flow differences in exploratory renderings of composite clouds from RCE_{on} (not shown).

As far as the authors are aware, there is no simple mathematical framework incorporating the NCT into the kind of mesoscale convective circulations in which we are interested. So, we now introduce one. Our goal in developing such a framework is to combine it with our simulations to provide generalizable insights into the impact of the NCT on convective circulations.

4. Effect of the Non-traditional Coriolis force on a general poloidal circulation

In this section we describe analytically the effect of the Coriolis force on an axisymmetric poloidal flow. Our first insight is to consider a general poloidal flow and compute the net Coriolis force experienced by this flow. Instead of providing an exact solution for the circulation, this method shows where the Coriolis force is felt within a circulation, and how that force depends on the latitude of the circulation.

Our second insight is to realize that in an incompressible or anelastic flow, the pressure adjusts instantaneously in order to yield a net force which is divergence-free. Even in a compressible flow, sound waves rapidly adjust the pressure field so that the net force rapidly becomes divergence-free. For incompressible fluids, the pressure (analagously, the geo-potential for atmospheric flows) is determined from the velocity field by inverting a Laplacian through what is called the Leray projection.

Although we will work on an f-plane, which means that we neglect the variation of the Coriolis force in our convective scales, we retain the latitudinal dependence of the Coriolis parameter so that we can describe the different effects of the net Coriolis force at different latitudes. Our analysis yields two structurally different net forces which the Coriolis force induces on a poloidal convective circulation, neither of which has any component in the vertical direction:

1. A toroidal force which is cyclonic in the axially confluent region of the circulation and anti-cyclonic in the axially diffluent region of the circulation. Its strength is proportional to the *sine* of the latitude, and thereby vanishes at the equator and is maximal at the poles. This is the effect of the traditional Coriolis force which induces a cyclonic/anti-cyclonic first baroclinic structure.

2. A force which is in the horizontal plane, having a dipolar, diffuluent structure around the center of convection. It acts westward (easterly) in the center of a convective updraft, recirculates poloidally away from the center, is maximal at the point of maximum vertical velocity, and varies as the *cosine* of latitude. These NCT effects are most pronounced at the equator, induce westward tilts in convective updrafts and diffluence at the top of the convective circulation.

a. The equations for the net Coriolis force

Consider the incompressible Euler equations (in vector form) in a stratified fluid in the presence of rotation (modeled by an f-plane),

$$\vec{u}_t + \vec{u} \cdot \vec{\nabla}\, \vec{u} + \vec{\nabla} p + 2\vec{\Omega} \times \vec{u} = B\hat{k} \tag{8}$$

$$\nabla \cdot \vec{u} = 0 \tag{9}$$

where

$$\vec{\Omega} = \Omega_0 \left[\cos(\phi)\hat{j} + \sin(\phi)\hat{k}\right] \tag{10}$$

$\hat{i}, \hat{j}, \hat{k}$ are the unit vectors in the local eastward, northward, and upward directions, respectively. The other symbols are the same as described in the previous sections. Equations (8) and (9) are the vector form of equations (1)-(4), and thereby contain, both, traditional and non-traditional Coriolis terms. The anelastic generalization of these equations would replace (9) with $\nabla\cdot(\rho(z)\vec{u}) = 0$, where $\rho(z)$ is a prescribed density stratification. While the details of the computation would change for the anelastic case, the principle of the Leray projection would remain.

The Leray projection provides the algorithm for determining the pressure from the force and circulation, thereby constructing the net, divergence-free force required to maintain a divergence-free flow, $\vec{u}$. By taking the divergence of (8) and substituting the time derivative of (9), the pressure can be determined by the inversion of the Laplacian

$$\nabla^2 p = \nabla\cdot\left[B\hat{k} - 2\vec{\Omega}\times\vec{u} - \vec{u}\cdot\nabla\vec{u}\right] \tag{11}$$

and thereby contains components due to buoyancy, the Coriolis force, and the fluid inertia, respectively. The boundary conditions for the pressure are determined by the boundary conditions for the flow. On a rigid boundary, the velocity field satisfies

$$\vec{u}\cdot\hat{n} = 0 \tag{12}$$

where $\hat{n}$ is the unit normal on the boundary. Taking the dot product of (8) with $\hat{n}$, evaluating it on a rigid boundary, and using (12) yields a Neumann boundary condition for the pressure on the boundary

$$\nabla p\cdot\hat{n} = \hat{n}\cdot\left[B\hat{k} - 2\vec{\Omega}\times\vec{u} - \vec{u}\cdot\nabla\vec{u}\right]. \tag{13}$$

This is simply the mathematical expression for the balance of forces at a rigid boundary; since the flow cannot penetrate a rigid boundary, the total normal force due to bouyancy, Coriolis, and fluid inertia must be balanced by the normal pressure gradient at a rigid boundary.

On a free boundary the boundary condition is simply continuity of pressure. In the atmosphere, we will consider a rigid lower boundary (which we will denote $z = 0$), and decay of pressure as $|vecx| \to \infty$.

The question we ask is, when considered at a fixed latitude and on scales appropriate to convective clouds, what is the *net* effect of *only* the Coriolis force on an idealized, axially symmetric, poloidal circulation. We leave to future work the discussion of the effect of the buoyancy, $B\hat{k}$, and inertia terms, $\vec{u} \cdot \vec{\nabla}\, \vec{u}$. Therefore we must solve for *the net Coriolis force* which results after the Leray projection, since in an incompressible flow, the pressure (geopotential) adjusts instantaneously to maintain the divergence-free constraint. To solve this problem involves projecting out the portion of the Coriolis force which contains divergence. Defining the net Coriolis force as

$$\vec{F} = -2\vec{\Omega} \times \vec{u} - \nabla p_{\mathrm{C}} \tag{14}$$

where p_{C}, we call the Coriolis pressure, is determined by requiring $\vec{F}$ to be divergence-free,

$$\nabla \cdot \vec{F} = 0 \quad \Longrightarrow \quad \nabla^2 p_C = -2\nabla \cdot \left[\vec{\Omega} \times \vec{u}\right]. \tag{15}$$

The Neumann boundary condition on p_C is results from requiring that the normal component of the net force $\vec{F} \cdot \hat{n}$ equal zero on $z = 0$

$$\frac{\partial p_C}{\partial z} = 2\hat{n} \cdot \left(\vec{\Omega} \times \vec{u}\right) \quad \text{on} \quad z = 0. \tag{16}$$

At large distances from the flow, the Coriolis force decays to zero, so we will require the pressure to decay to zero, also.

b. Computing the Coriolis pressure

Now we construct the Coriolis pressure in $(x,y) \in \mathbf{R}^2$, $z \geq 0$. The Coriolis pressure is the portion of the total pressure field arising from the Coriolis force acting on the velocity field of concern, in our case a poloidal flow which satisfies (15) and boundary conditions (16). To simplify the right hand side of equation (15) we use the vector identity $\vec{\nabla} \cdot \left[\vec{\Omega} \times \vec{u}\right] = \left(\vec{\nabla} \times \vec{\Omega}\right) \cdot \vec{u} - \left(\vec{\nabla} \times \vec{u}\right) \cdot \vec{\Omega}$. The rotation vector is constant and the vorticity is defined as the curl of the velocity field $\vec{\omega} = \vec{\nabla} \times \vec{u}$ so equation (15) becomes

$$\nabla^2 p_C = 2\vec{\Omega} \cdot \vec{\omega}. \tag{17}$$

In the following, we will show that, for axially symmetric poloidal flows, the Laplacian in (17) is explicitly invertable and yields an analytic description of the Coriolis pressure in terms of the Stokes Stream Function (Stokes (1842)) of the poloidal flow.

c. Circularly symmetric poloidal circulation

Since the vorticity field of a circularly symmetric poloidal circulation is purely toroidal, it behooves us to compute the basis vectors in cylindrical polar coordinates as a function of angle in the plane, and expressed in terms of the Cartesian basis. Clearly the vertical direction is the same in both coordinate systems and we need only express

$$\begin{aligned} \hat{r} &= \cos(\theta)\hat{i} + \sin(\theta)\hat{j} \\ \hat{\theta} &= -\sin(\theta)\hat{i} + \cos(\theta)\hat{j}, \end{aligned} \tag{18}$$

being the axially outward, toroidal unit vectors, respectively.

Focusing on general axisymmetric, poloidal, incompressible circulations, we consider a local cylindrical coordinate system in which the velocity is written in component form as

$$\vec{u} = u_r(r,z)\,\hat{r} + u_\theta(r,z)\,\hat{\theta} + u_z(r,z)\,\hat{k}. \tag{19}$$

The poloidal nature of the flow implies $u_\theta = 0$ and axisymmetry implies $\partial u_r/\partial\theta = \partial u_z/\partial\theta = 0$. Incompressibility of the flow in the (r,z)-plane yields the divergence-free constraint for $\vec{u}$ in that plane,

$$\frac{1}{r}\frac{\partial(ru_r)}{\partial r} + \frac{\partial u_z}{\partial z} = 0. \tag{20}$$

Any divergence-free vector field can be expressed as the curl of a vector potential, so we can express the toroidally symmetric poloidal flow, $\vec{u}$ as

$$\vec{u} = \nabla\times\left(\Psi\hat{\theta}\right) \tag{21}$$

where $\vec{\Psi} = \Psi(r,z)\hat{\theta}$ is the (divergence-free) vector potential, in analogy to the vector potential of magnetostatics. Since we will only consider poloidal circulations, and thereby toroidal vector potentials for the remainder of the discussion, hereafter we will refer to the scalar function Ψ as the vector potential - despite the fact that it is actually the magnitude of the vector potential. Using Ψ, the components of the poloidal velocity field are

$$u_r = -\frac{\partial\Psi}{\partial z}, \quad u_\theta = 0, \quad u_z = \frac{1}{r}\frac{\partial(r\Psi)}{\partial r}. \tag{22}$$

Although Ψ has the dimensions of a stream function, the flow is not tangent to contours of Ψ.

The "Stokes Stream function" (Stokes 1842) is designed so that its contours are tangent to the vector field of the flow. For poloidal flows in cylindrical coordinates, the Stokes Stream function, ψ, is equal to the distance from the axis multiplied by the toroidal component of the vector potential,

$$\psi = r\Psi. \tag{23}$$

Substituting (23) into (22) we find

$$\vec{u} = \frac{1}{r}\left[-\frac{\partial\psi}{\partial z}\hat{r} + \frac{\partial\psi}{\partial r}\hat{k}\right], \tag{24}$$

the velocity field is everywhere tangent to contours of ψ, but proportional in magnitude to $\frac{|\nabla\psi|}{r}$.

The Coriolis force is computed using the vector potential Ψ from equation (21) or (22) and the rotation vector from equation (10),

$$\begin{aligned}
-2\vec{\Omega}\times\vec{u} &= -2\Omega_0\left[\cos(\phi)\hat{j}+\sin(\phi)\hat{k}\right]\times\left[-\frac{\partial\Psi}{\partial z}\hat{r}+\frac{1}{r}\frac{\partial(r\Psi)}{\partial r}\hat{k}\right] \\
&= -2\Omega_0\left[\cos(\phi)\sin(\theta)\hat{r}+\cos(\phi)\cos(\theta)\hat{\theta}+\sin(\phi)\hat{k}\right]\times\left[-\frac{\partial\Psi}{\partial z}\hat{r}+\frac{1}{r}\frac{\partial(r\Psi)}{\partial r}\hat{k}\right] \\
&= -2\Omega_0\left\{\cos(\phi)\left[-\frac{\sin(\theta)}{r}\frac{\partial(r\Psi)}{\partial r}\hat{\theta}+\cos(\theta)\frac{\partial\Psi}{\partial z}\hat{k}+\frac{\cos(\theta)}{r}\frac{\partial(r\Psi)}{\partial r}\hat{r}\right]\right. \\
&\qquad\left.-\sin(\phi)\frac{\partial\Psi}{\partial z}\hat{\theta}\right\}.
\end{aligned} \tag{25}$$

The $\hat{k}$ component of this force is needed to determine the boundary condition on the Coriolis pressure. Using equation (25) in (16) we find

$$\frac{\partial p_C}{\partial z} = -2\Omega_0\cos(\phi)\cos(\theta)\,\frac{\partial\Psi}{\partial z} \quad \text{on} \quad z=0. \tag{26}$$

The vorticity of an axisymmetric poloidal flow is purely in the toroidal direction,

$$\vec{\omega} = \left[\frac{\partial u_r}{\partial z}-\frac{\partial u_z}{\partial r}\right]\hat{\theta} \tag{27}$$

which, when expressed in terms of the vector potential, Ψ, becomes

$$\begin{aligned}
\vec{\omega} &= -\left[\frac{\partial}{\partial r}\left(\frac{1}{r}\frac{\partial(r\Psi)}{\partial r}\right)+\frac{\partial^2\Psi}{\partial z^2}\right]\hat{\theta} \\
&= -\left[\frac{\partial}{\partial r}\left(\frac{\partial\Psi}{\partial r}+\frac{\Psi}{r}\right)+\frac{\partial^2\Psi}{\partial z^2}\right]\hat{\theta} \\
&= -\left[\frac{\partial^2\Psi}{\partial r^2}+\frac{1}{r}\frac{\partial\Psi}{\partial r}-\frac{\Psi}{r^2}+\frac{\partial^2\Psi}{\partial z^2}\right]\hat{\theta}.
\end{aligned} \tag{28}$$

The reader may note that $\vec{\omega}=-\nabla^2\vec{\Psi}$, the vector Laplacian of the vector potential; we could use this identity to solve for the Coriolis pressure, but we take the more brute force approach for the sake of clarity.

Taking the dot product of the toroidal vorticity equation (28), with the equation for the rotation vector (10), yields a simple expression for the right hand side of Poisson's equation (17) for the

Coriolis pressure in terms of the vector potential,

$$\begin{aligned}
&\nabla^2 p_C = 2\vec{\Omega}\cdot\vec{\omega} \\
\Longrightarrow\ &\nabla^2 p_C = -2\Omega_0 \cos(\phi)\cos(\theta)\left[\frac{\partial^2\Psi}{\partial r^2} + \frac{1}{r}\frac{\partial\Psi}{\partial r} - \frac{\Psi}{r^2} + \frac{\partial^2\Psi}{\partial z^2}\right].
\end{aligned} \tag{29}$$

d. Solving for the Coriolis pressure

We are left to solve equation (29) with the $z = 0$ boundary condition given in equation (26). In cylindrical coordinates, the Laplacian of the Coriolis pressure is expressed as

$$\nabla^2 p_C = \frac{\partial^2 p_C}{\partial r^2} + \frac{1}{r}\frac{\partial p_C}{\partial r} + \frac{1}{r^2}\frac{\partial^2 p_C}{\partial\theta^2} + \frac{\partial^2 p_C}{\partial z^2}. \tag{30}$$

The absolutely elegant fact is that the solution of (29) is *extremely simple*. To solve for p_C, we introduce the function $P(r,z)$ and substitute

$$p_C(r,\theta,z) = P(r,z)\ \cos(\theta) \tag{31}$$

into equation (29) using the identity from equation (30) to arrive at

$$\left[\frac{\partial^2 P}{\partial r^2} + \frac{1}{r}\frac{\partial P}{\partial r} - \frac{P}{r^2} + \frac{\partial^2 P}{\partial z^2}\right]\cos(\theta) = -2\Omega_0 \cos(\phi)\cos(\theta)\left[\frac{\partial^2\Psi}{\partial r^2} + \frac{1}{r}\frac{\partial\Psi}{\partial r} - \frac{\Psi}{r^2} + \frac{\partial^2\Psi}{\partial z^2}\right]. \tag{32}$$

In general, we would have to invert the linear operator on the left hand side of this expression to solve for P - but the simplicity of this equation allows us to read off the solution without any more work. Notice that the dependence on θ and the differential operator is the same on the right and left hand sides of equation (32). Therefore P is proportional to Ψ plus an, as of yet undetermined function, R. So we have found $P(r,z) = -2\Omega_0 \cos(\phi)\ [\Psi(r,z) + R(r,z)]$, where R is a homogeneous solution of the differential operator in equation (32). The resulting Coriolis pressure is expressed explicitly in terms of Ψ and R as

$$p_C(r,z,\theta) = -2\Omega_0 \cos(\phi)\ [\Psi(r,z) + R(r,z)]\cos(\theta). \tag{33}$$

Upon taking the z-derivative of p_C in equation (33) and substituting the derivative into the boundary condition (26) we arrive at the boundary condition for R

$$\frac{\partial R}{\partial z} = 0 \quad \text{on} \quad z = 0. \tag{34}$$

We conclude that, since R is a solution to a homogeneous elliptic partial differential equation with homogeneous boundary conditions, therefore $R(r,z) = 0$ everywhere. Thus the Coriolis pressure, p_C, is given by the expression in (33) with $R = 0$.

e. Solving for the net Coriolis force

The negative gradient of the Coriolis pressure (33) is

$$-\vec{\nabla} p_c = 2\Omega_0 \cos(\phi) \left[\frac{\partial \Psi}{\partial r} \cos(\theta) \hat{r} - \frac{\Psi \sin(\theta)}{r} \hat{\theta} + \frac{\partial \Psi}{\partial z} \cos(\theta) \hat{k} \right]. \tag{35}$$

To this expression we add the Coriolis force in (25) to arrive at the net Coriolis force from equation (14) expressed in terms of the vector potential, Ψ,

$$\vec{F}_{\text{net}} = 2\Omega_0 \left\{ -\cos(\phi) \left[\frac{\Psi}{r} \cos(\theta) \hat{r} - \frac{\partial \Psi}{\partial r} \sin(\theta) \hat{\theta} \right] + \sin(\phi) \left[\frac{\partial \Psi}{\partial z} \hat{\theta} \right] \right\}. \tag{36}$$

Notice that vertical component of the net force *vanishes everywhere* in r, θ for $z > 0$, not just at the lower boundary. This result was not obvious before we embarked upon the calculation, since the Coriolis force does have a vertical component throughout the fluid (notice the $\hat{k}$ component of the force in equation 25). Nonetheless, we have shown that the component of the Coriolis force associated with the eastward component of the velocity balances the vertical gradient of the Coriolis pressure (refer to equation (3)), at least away from the poles where $\cos(\phi) = 0$.

The remarkably straightforward result in equation (36) can actually be further simplified. Using the polar coordinate representation of the curl, we can write the first term in parenthesis as

$$\begin{aligned}
-\left[\frac{\Psi}{r}\cos(\theta)\hat{r}-\frac{\partial\Psi}{\partial r}\sin(\theta)\,\hat{\theta}\right] &= \vec{\nabla}\times\left(-\Psi(r,z)\sin(\theta)\,\hat{k}\right)\\
&= \vec{\nabla}\times\left(-G(x,y,z)\,\hat{k}\right)\\
&= -\frac{\partial G}{\partial y}\,\hat{i}+\frac{\partial G}{\partial x}\,\hat{j}\\
&\equiv \nabla^{\perp}G
\end{aligned} \tag{37}$$

where

$$G = \Psi\,\sin(\theta) \tag{38}$$

and $\nabla^{\perp}$ is the perpendicular gradient, which is equivalent to the tangential derivative; $\nabla^{\perp}G$ is a vector field directed clockwise around maxima of G.

Substituting this result into the expression for the net force (36) we arrive at the main result of our analysis

$$\vec{F}_{\text{net}} = 2\Omega_0\left\{\cos(\phi)\nabla^{\perp}\left[\Psi\sin(\theta)\right]+\sin(\phi)\frac{\partial\Psi}{\partial z}\,\hat{\theta}\right\}, \tag{39}$$

whose interpretation follows.

1) Interpretation of the $\sin(\phi)$ term; Coriolis Rotation

The second term in equation (39) is proportional to the sine of latitude, so that it vanishes at the equator, is antisymmetric about the equator, and is maximal at the poles. This term is due to the traditional Coriolis force and acts solely in the toroidal direction.

Since the force is proportional to

$$\vec{F}_{\text{net},2} \propto \frac{\partial\Psi}{\partial z} \propto -u_r, \tag{40}$$

we note that it is proportional to the negative of the radial velocity. This expression tells us that at elevations of maximal radial inflow, there is a maximal force in the cyclonic direction, whereas at elevations of maximal radial outflow, there is a maximal anti-cyclonic force. This force would tend to spin a convective cell cyclonically near the base of the troposphere and anti-cyclonically near the tropopause.

We name this the Coriolis Rotation term. It will likely feel familiar to readers.

2) Interpretation of the $\cos(\phi)$ term; Coriolis Shear

The first term in parenthesis in equation (39) is more subtle, more interesting, and in our opinion, not adequately discussed in the literature. It is symmetric about the equator, so there is no hemispheric difference in its effects. It is also maximum at the equator and vanishes at the poles.

Since it depends on the (x, y) perpendicular gradient of the function $G = \Psi \sin(\theta)$, contours of G are related to the divergence-free, net Coriolis force in the same way that a stream function in two dimensions is related to an incompressible velocity field. That is to say the force is tangent to contours of constant G, and where G changes sharply, the force is strongest. We reiterate that, from the definition of the perpendicular gradient in (37), it is clear that the force vectors swirl counterclockwise around low values of G. Importantly, this sense of circulation of the force vectors is independent of latitude, unlike the Coriolis rotation term whose sign changes across the equator.

We name this component of the force, the Coriolis Shear term and G, from equation (38), we name the Shear Potential.

5. The net Coriolis force associated with the "DoNUT" Model of convective circulation

An elucidating model for a poloidal circulation is what we have called the "DoNUT" Model (the "Dynamics of Non-rotating Updraft Torii"). This is a model we will introduce here and describe more completely in future work. For now, the simplest DoNUT is described by a vector potential which is separable in r and z (in $z \geq 0$), and independent of θ. An example of such a flow contains two length scales, L, H, and a strength, w_*,

$$\Psi(r,z) = \frac{w_*}{2}\,\frac{rz}{H}\,e^{1-\frac{z}{H}-\frac{2r}{L}}. \tag{41}$$

To understand the physical meaning of these parameters, we compute the vertical velocity

$$\begin{aligned} u_z &= \frac{1}{r}\frac{\partial(r\Psi)}{\partial r} \\ &= w_*\,\frac{z}{H}\,\left[1-\frac{r}{L}\right]e^{1-\frac{z}{H}-\frac{2r}{L}}, \end{aligned} \tag{42}$$

and radial velocity

$$\begin{aligned} u_r &= -\frac{\partial\Psi}{\partial z} \\ &= -\frac{w_*}{2}\,\frac{r}{H}\,\left[1-\frac{z}{H}\right]e^{1-\frac{z}{H}-\frac{2r}{L}}. \end{aligned} \tag{43}$$

Therefore the flow described by (41) consists of a radially inward velocity below $z = H$, and a radially outward velocity above $z = H$. The maximum magnitude of the radial velocity occurs at $z = 0$ in the DoNUT, and the magnitude decreases as $r \to \infty$.

The vertical velocity is positive for $r < L$ and negative for $r > L$. The vertical velocity is maximum on the axis of symmetry, increases from the ground ($z = 0$), reaches a maximum of $u_{z,\max} = w_*$ at height $z = H$, and decreases to zero as $z \to \infty$.

In figure 5, we plot the DoNUT's Stokes Stream Function, $\psi = r\Psi$ in coordinates $(r/L, z/H)$. By scaling (L, H, w_*) a whole family of different flows can be described by (41).

Of the two net forces we have described, Coriolis Rotation and Coriolis Shear, the second is the less intuitive and is the one that needs more description. Computing the Shear Potential (38) associated with the DoNUT (41) we find

$$G(x,y,z) = \frac{w_*}{2}\,\frac{yz}{H}\,e^{1-\frac{z}{H}-\frac{2\sqrt{x^2+y^2}}{L}}. \tag{44}$$

We have expressed G in Cartesian coordinates since the tangential gradient, $\nabla^\perp$, is most easily described in Cartesian variables. The Coriolis Shear force is purely in the (x, y) plane and is derived from the (x, y) derivatives of the Shear Potential. Therefore, the z-dependent terms in the Shear Potential act together as a scale factor for the strength of the force at each height. The vertical velocity on the axis of symmetry ($r = 0$) is also the maximum velocity at each height,

$$w(z) \equiv w_* \frac{z}{H} e^{1-\frac{z}{H}}, \tag{45}$$

which, itself, attains the maximum w_* at $z = H$. This identification allows us to write (44) as

$$G = w(z) \frac{y}{2} e^{-\frac{2\sqrt{x^2+y^2}}{L}}. \tag{46}$$

From this expression, we learn that the maximum Coriolis Shear occurs at the height of the maximum vertical velocity. In a separable stream function, the strength of the Coriolis Shear at any height is proportional to the strength of the vertical velocity along the axis of symmetry at that height - this is the updraft velocity.

Along the axis of symmetry, the net Coriolis Shear force, which is the term proportional to $\cos(\phi)$ in equation (39), is

$$\vec{F}_{\mathrm{CS}}(0, z) = -2\Omega_0 \cos(\phi) \frac{\partial G}{\partial y} \hat{\imath} = -\Omega_0 \cos(\phi)\, w(z)\, \hat{\imath} \tag{47}$$

If the central vertical velocity is upward, then this Coriolis Shear force along the axis is westward and proportional in strength to the vertical velocity along the axis. Therefore the Coriolis Shear force imparts a westward tilt to the convective towers and is most pronounced near the equator.

Figure 6 shows contours of G and vectors of the Coriolis Shear for the DoNUT circulation. Motion is upward at the origin. The westward force at the convective core and along the latitude of the convective core is clearly visible. The lines of force also circulate as a dipole centered along the axis of symmetry. This circulating force can impart spreading throughout the convective column but is most strongly felt at the height of maximum vertical velocity.

a. Simulating the DoNUT

Having gone through this development with due rigor, we are left wondering whether we can recreate these results with more RAMS simulations. The DoNUT model is steady-state. To reflect this, we run a set of RAMS simulations with a surface enthalpy flux that varies in space but is constant in time. The flux occurs over a double-Gaussian patch in the center of the domain with a full half width of 5km. The maximum flux is 500W m^{-2}. Microphysics is turned off for simplicity. The two simulations are DONUT$_{off}$ and DONUT$_{on}$. They are run for 3 hours. An ascending plume sets up over the enthalpy flux patch while the rest of the domain is characterized by far-field descent. The flow characteristics of the convective circulation in DONUT$_{on}$ can be seen in Fig. 7a/c. The flows shown have been averaged horizontally (in Fig. 7a/b) over the middle 5km and vertically (in Fig. 7c/d) between 5km and 7km height and over the final 30 minutes of the simulations.

Figure 7d shows the difference in the horizontal flow (DONUT$_{on}$ minus DONUT$_{off}$) after 3 hours. While we cannot calculate the force from the model in a way that would be identical to the DoNUT model, we can instead show the resulting flow which proves to be remarkably consistent with that implied by the force in Fig. 6. RAMS simulates westward acceleration (as it does in NCT$_{on}$ and RCE$_{on}$) and the meridional confluence and difluence pattern predicted by the DoNUT model.

6. Summary

Above, we asked what, in some senses, is a question with an obvious answer: might equatorial deep convective clouds feel an impact from the Non-traditional Coriolis Terms (NCT)? Intuition may suggest that the answer is “no” given the relative slowness of the rotation of the Earth and the relative fastness of convection. Perhaps surprisingly, then, we have shown that the answer is more likely “yes”. Taken as a whole, why do we suggest this?

1. Vertical wind speeds are weak and the tropical troposphere is (relatively) deep. A simple scaling argument which depends on the relatively weak 10m/s updrafts in tropical convection and relatively deep convective layer of 18km results in a 2.4km zonal displacement of an isolated ascending parcel. This suggests that convective plumes should tilt systematically to the west at 7.5° relative to the vertical. Westward tilts occur at or on either side of the equator.

2. Our use of a poloidal model of convection (introduced as the “DoNUT” model) to characterize the entire convective circulation links fast convective processes which may be marginally impacted by the Coriolis force on a slowly rotating planet with slow compensating decent which occurs on a much longer timescale. The latter intuitively are more deflected by the Coriolis force.

3. The NCT affects circulations potentially weakly, but always systematically, due in part to the rigid surface which introduces symmetry breaking. We also suspect, although do not make any attempt to show, that the impact of turbulent dissipation which will be much larger in convecting centers than in subsiding environments also introduces another source of asymmetric impacts from the NCT.

In order to illustrate the impact of these simple mathematical arguments, we added the NCT to RAMS and ran three groups of simulations. The first was a small ensemble of congestus simulations. The impact of the NCT was to preferentially lift air with positive zonal momentum. The second was a set of restarted RCE simulations. There, we showed that convective velocities are weakened (in a statistical sense) and that the morphology of surface precipitation is characteristically altered by the NCT. The third was of steady-state convection occurring due to a patch of enhanced surface enthalpy flux. The NCT resulted in a different overturning structure in the vertical plane and the confluence-difluence couplet suggested by our poloidal "DoNUT model" in the horizontal plane.

As a practical suggestion, we think it is reasonable to include the NCT in cloud resolving models; we see no reason to exclude it given the low computational burden of including it. That is not to say it should be used in all simulations just as the traditional terms are often excluded intentionally in simulations. We would also suggest that systematic tilts to convective storms, of the sort suggested above, could be observable in vertically-resolved cloud data if suitably shear-free conditions can be found. Unfortunately, current satellite instruments are locked in predominantly-north-south orbits which would largely preclude their providing useful observation.

Data availability statement. Data used in figures are available (for reviewer preview) at: https://datadryad.org/stash/share/NWrmFVpJBZtm3D8rB2xin1-DU9n8eXGPftbSaDqttak .

Acknowledgments. MRI would like to thank his recent ATM121A classes who dealt with the NCT on various exams. MRI would also like to acknowledge startup funding from the University of California Davis. MRI and JAB conceived the work. MRI ran and analyzed simulations. JAB performed the mathematically analysis. MRI and JAB wrote the manuscript.

JAB would like to dedicate his effort in this work to the memory of Dr. René Samson, formerly of M.I.T. and the Shell Corporation. René's mathematical insights, impeccable mathematical and artistic taste, and his drive for understanding made him a great Renaissance man and an inspiration to those who met him.

References

Bryan, G. H., 2015: The governing equations for CM1.

Busse, F., 1976: A simple model of convection in the Jovian atmosphere. *Icarus*, **29 (2)**, 255–260, doi:10.1016/0019-1035(76)90053-1, URL https://linkinghub.elsevier.com/retrieve/pii/0019103576900531.

Ciesielski, P. E., and Coauthors, 2014: Quality-Controlled Upper-Air Sounding Dataset for DYNAMO/CINDY/AMIE: Development and Corrections. *Journal of Atmospheric and Oceanic Technology*, **31 (4)**, 741–764, doi:10.1175/JTECH-D-13-00165.1, URL http://journals.ametsoc.org/doi/abs/10.1175/JTECH-D-13-00165.1.

Colin, M., S. Sherwood, O. Geoffroy, S. Bony, and D. Fuchs, 2018: Identifying the Sources of Convective Memory in Cloud-Resolving Simulations. *Journal of the Atmospheric Sciences*, **76 (3)**, 947–962, doi:10.1175/jas-d-18-0036.1.

Cotton, W. R., and Coauthors, 2003: RAMS 2001: Current status and future directions. *Meteorology and Atmospheric Physics*, **82**, 5–29, doi:10.1007/s00703-001-0584-9.

de Coriolis, G.-G., 1835: Memoire sur les equations du mouvement relatif des systemes de corps. *Journal Ecole Polytechnique*, **XXIV (XV)**, 142–154.

Denbo, D. W., and E. D. Skyllingstad, 1996: An ocean large‐eddy simulation model with application to deep convection in the Greenland Sea. *Journal of Geophysical Research: Oceans*, **101 (C1)**, 1095–1110, doi:10.1029/95JC02828, URL http://doi.wiley.com/10.1029/95JC02828.

Dintrans, B., M. Rieutord, and L. Valdettaro, 1999: Gravito-inertial waves in a rotating stratified sphere or spherical shell. *Journal of Fluid Mechanics*, **398**, 271–297, doi:10.1017/S0022112099006308, URL https://www.cambridge.org/core/product/identifier/S0022112099006308/type/journal{_}article.

Gerkema, T., J. T. Zimmerman, L. R. Maas, and H. Van Haren, 2008: Geophysical and astrophysical fluid dynamics beyond the traditional approximation. *Reviews of Geophysics*, **46 (2)**, 1–33, doi: 10.1029/2006RG000220.

Hayashi, M., and H. Itoh, 2012: The Importance of the Nontraditional Coriolis Terms in Large-Scale Motions in the Tropics Forced by Prescribed Cumulus Heating. *Journal of the Atmospheric Sciences*, **69 (9)**, 2699–2716, doi:10.1175/jas-d-11-0334.1.

Igel, A. L., M. R. Igel, and S. C. van den Heever, 2015: Make It a Double? Sobering Results from Simulations Using Single-Moment Microphysics Schemes. *Journal of the Atmospheric Sciences*, **72 (2)**, 910–925, doi:10.1175/JAS-D-14-0107.1, URL http://journals.ametsoc.org/doi/10.1175/JAS-D-14-0107.1.

Igel, M. R., 2018: Lagrangian Cloud Tracking and the Precipitation-Column Humidity Relationship. *Atmosphere*, **9**, 289, doi:10.3390/atmos9080289.

Kasahara, A., 2003: On the Nonhydrostatic Atmospheric Models with Inclusion of the Horizontal Component of the Earth's Angular Velocity. *Journal of the Meteorological Society of Japan*, **81**, 935 – 950.

Marshall, J., and F. Schott, 1999: Open-ocean convection: Observations, theory, and models. *Reviews of Geophysics*, **37 (1)**, 1–64, doi:10.1029/98RG02739, URL http://doi.wiley.com/10.1029/98RG02739.

Ogilvie, G. I., and D. N. C. Lin, 2004: TIDAL DISSIPATION IN ROTATING GIANT PLANETS. *The Astrophysical Journal*, **610**, 477–509.

Ong, H., and P. E. Roundy, 2019: Linear effects of nontraditional Coriolis terms on intertropical convergence zone forced large-scale flow. *Quarterly Journal of the Royal Meteorological Society*, qj.3572, doi:10.1002/qj.3572, URL https://onlinelibrary.wiley.com/doi/abs/10.1002/qj.3572.

Poisson, S. D., 1838: Sur le mouvement des Projectiles dans l'air, en ayant egard a la rotation de le terre. *Journal de l'Ecole Polytechnique*, **xvi**, 1–226.

Saleeby, S. M., and W. R. Cotton, 2004: A large-droplet mode and prognostic number concentration of cloud droplets in the Colorado State University Regional Atmospheric Modeling System (RAMS). Part I: Module descriptions and supercell test simulations. *Journal of Applied Meteorology*, **43**, 182–195, doi:10.1175/1520-0450(2004)043,0182:ALMAPN.2.0.CO;2.

Saleeby, S. M., and W. R. Cotton, 2008: A binned approach to cloud-droplet riming implemented in a bulk microphysics model. *Journal of Applied Meteorology and Climatology*, **47**, 694–703, doi:10.1175/2007JAMC1664.1.

Saleeby, S. M., and S. C. van den Heever, 2013: Developments in the CSU-RAMS aerosol model: Emissions, nucleation, regeneration, deposition, and radiation. *Journal of Applied Meteorology and Climatology*, **52**, 2601–2622, doi:10.1175/JAMC-D-12-0312.1.

Satoh, M., T. Matsuno, H. Tomita, H. Miura, T. Nasuno, and S. Iga, 2010: Nonhydrostatic icosahedaral atmospheric model (NICAM) for global cloud resolving simulations. *Journal of Computational Physics*, D00H14, URL http://doi:10.1029/2009JD012247.

Savonije, G. J., and J. C. B. Papaloizou, 1997: Non-adiabatic tidal forcing of a massive, uniformly rotating star – II. The low-frequency, inertial regime. *Monthly Notices of the Royal Astronomical Society*, **291 (4)**, 633–650, doi:10.1093/mnras/291.4.633, URL https://doi.org/10.1093/mnras/291.4.633.

Stokes, G., 1842: On the steady motion of incompressible fluids. *Transactions of the Cambridge Philosophical Society*, **7**, 439 – 453.

Tort, M., and T. Dubos, 2014: Dynamically consistent shallow-atmosphere equations with a complete Coriolis force. *Quarterly Journal of the Royal Meteorological Society*, **140 (684)**, 2388–2392, doi:10.1002/qj.2274.

LIST OF FIGURES

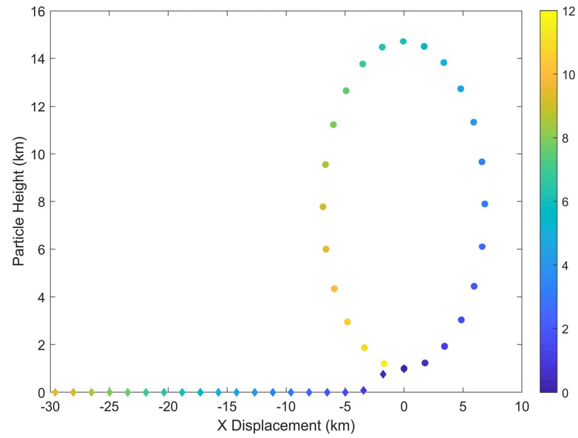

Fig. 1. Illustration of the evolution of a pair of arbitrary neutral air parcels under the influence of the Non-traditional Coriolis Terms. Marked locations indicate the evolution in space. Colors represent the evolution in time (colors darken as time increases). Circles show a parcel with $U_0 = 1\mathrm{ms}^{-1}$. Diamonds show a parcel with $U_0 = -1\mathrm{ms}^{-1}$.

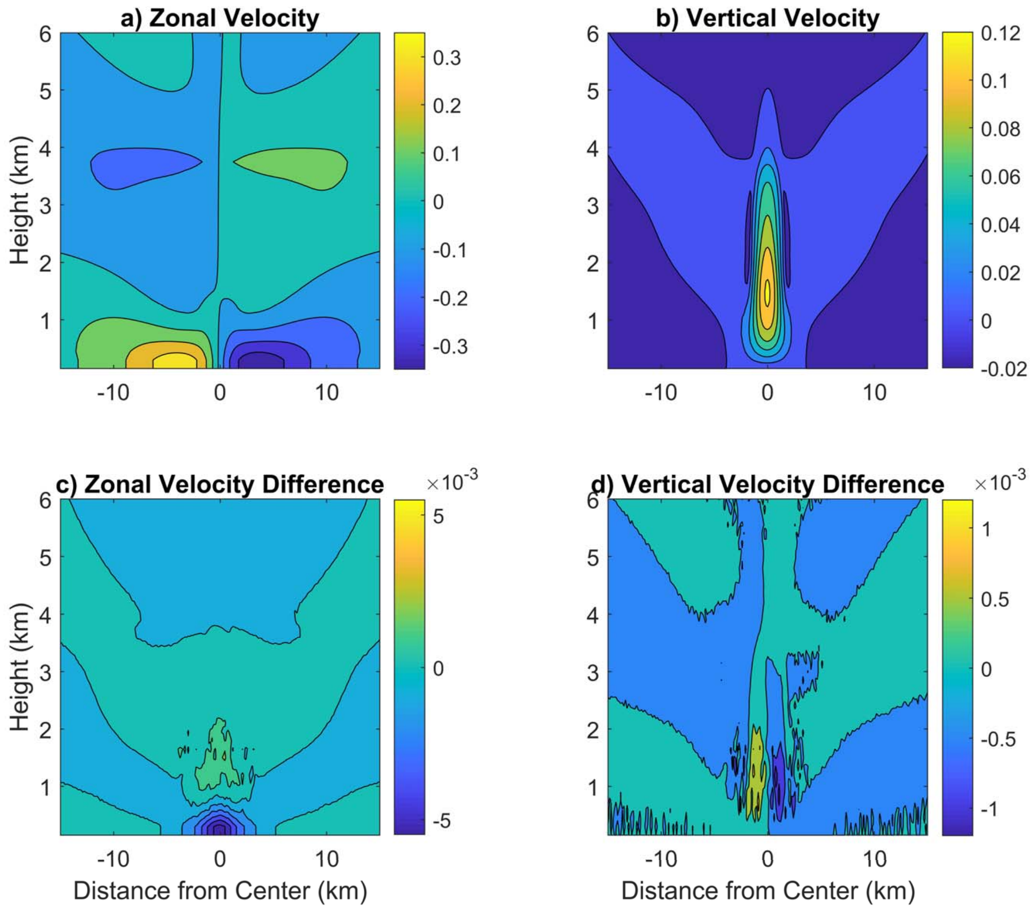

599 Fig. 2. Vertical cross-sections of velocity (in NCT$_{on}$) and velocity differences (as NCT$_{on}$ minus NCT$_{off}$). a) Zonal velocity through the the convergence center in NCT$_{on}$. b) Vertical velocity in NCT$_{on}$. c) Zonal velocity enhancement in NCT$_{on}$. d) Vertical velocity enhancement in NCT$_{on}$

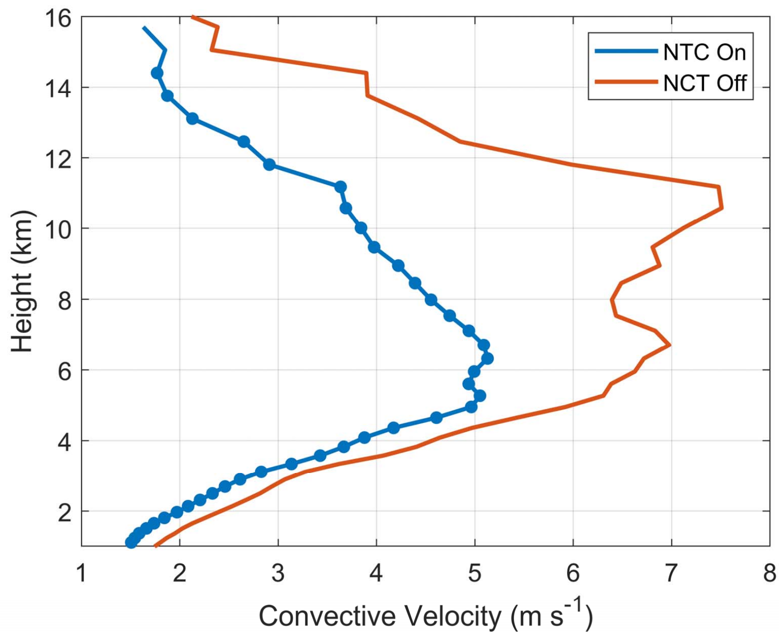

602 Fig. 3. Profiles of mean convective (i.e. $> 1\mathrm{ms}^{-1}$) vertical velocity in $\mathrm{RCE_{on}}$ and $\mathrm{RCE_{off}}$. Filled circles
603 indicate model levels where the statistical distributions of convective vertical velocities are distiguishable from
604 one another by a two sided t-test at the 99 % level.

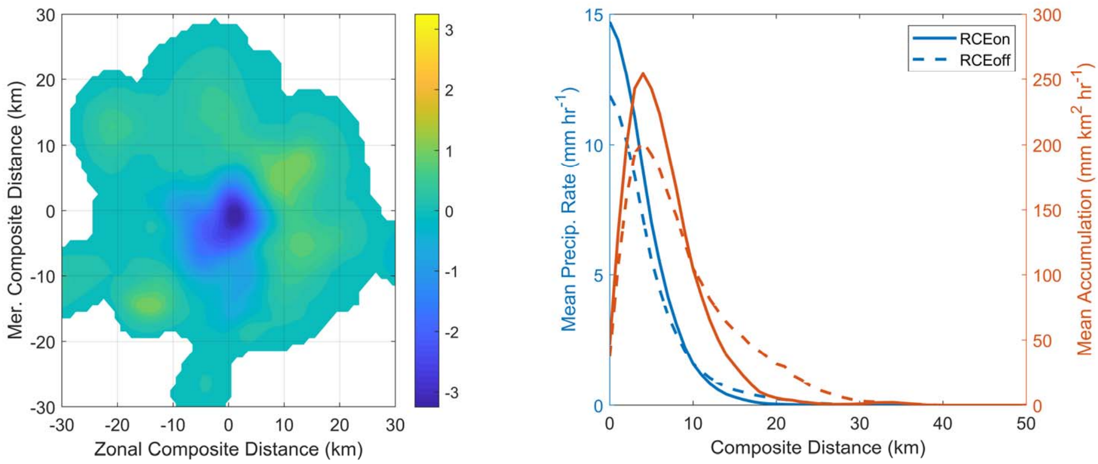

FIG. 4. a) Composite precipitation anomaly in RCE_{on} with units of mm/hr. The most intense instantaneous precipitation is used as the center point for all storms that contribute to the composite. b) The axisymmetrized composite of precipitation intensity (blue) and the axial accumulated precipitation (red).

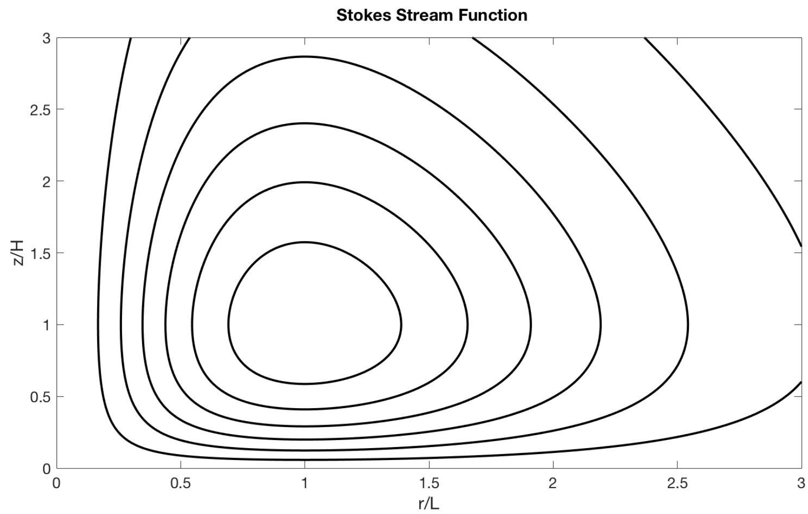

FIG. 5. Contours of the Stokes Stream function versus $(r/L, z/H)$ for the DoNUT Model of equation (41).

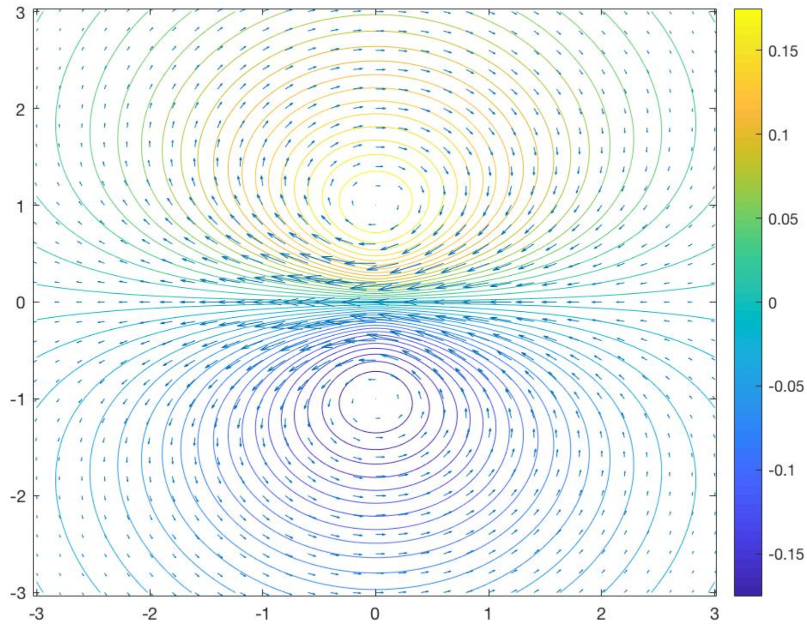

608 FIG. 6. The shear potential and force vectors as a function of (x, y) evaluated at elevation $z = H$ for the Shear Potential, G, from equation (46)

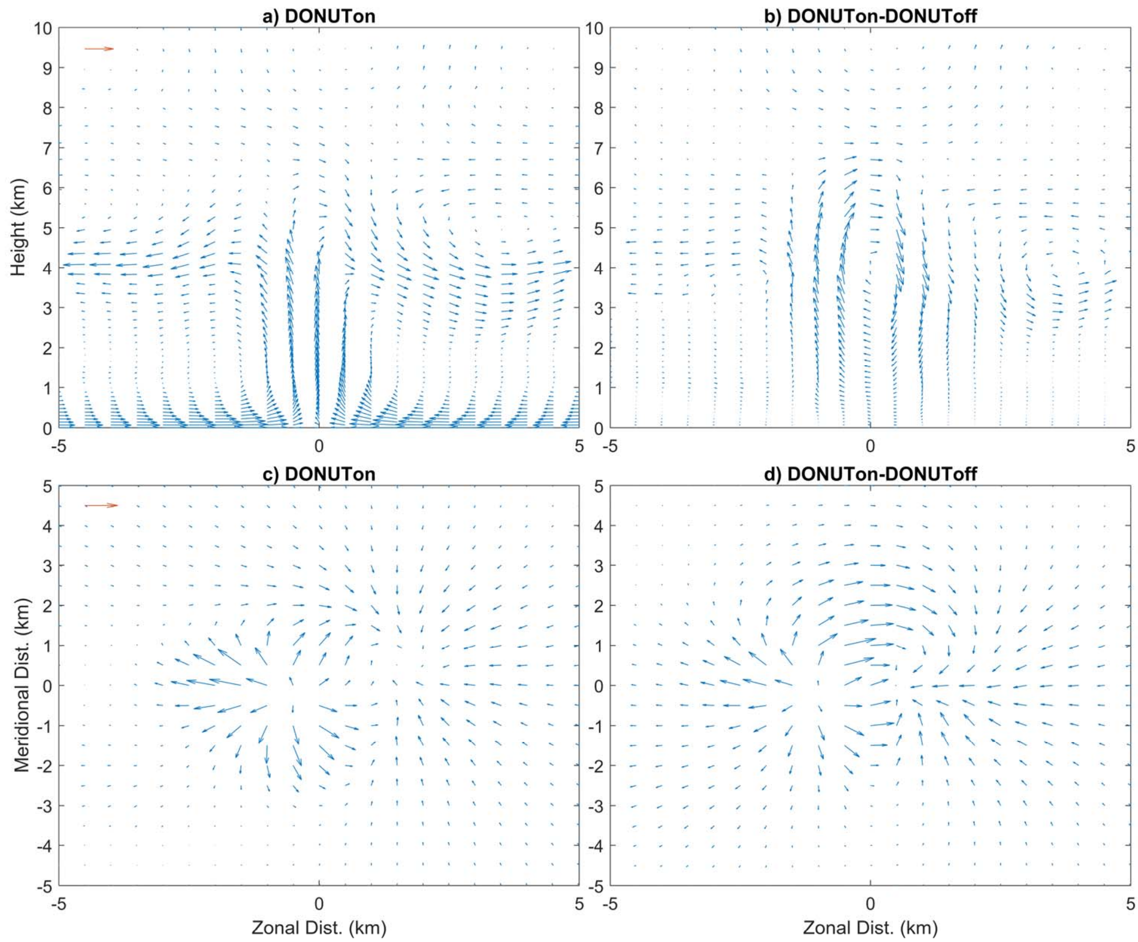

FIG. 7. Vectors indicate the magnitude of the respective two-dimensional flow. The top row shows zonal-vertical cross-sections along the axis of convergence averaged over 3km into and out of the page. The bottom row shows horizontal cross-sections at Red vectors illustrate a magnitude of $9\,\mathrm{ms}^{-1}$ which is approximately the largest magnitude vector in each panel